Journal of Materials Chemistry C

Accepted Manuscript

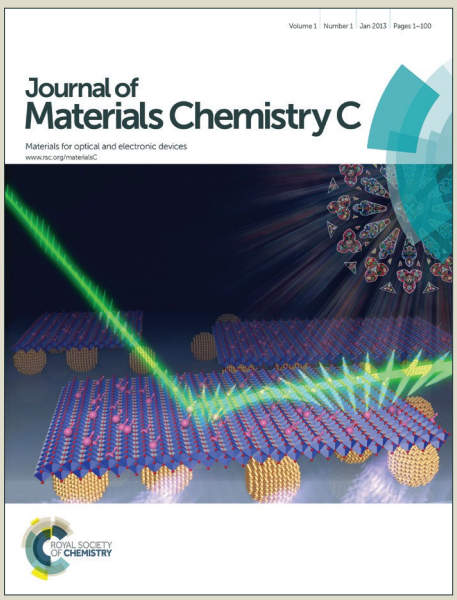

ROYAL SOCIETY OF CHEMISTRY

www.rsc.org/materialsC

Article type: Paper

Monolithic Graded-Refractive-Index Glass-based Antireflective Coatings: Broadband/Omnidirectional Light Harvesting and Self-Cleaning Characteristics

Tolga Aytug, Andrew R. Lupini, Gerald E. Jellison, Pooran C. Joshi, Ilia H. Ivanov, Tao Liu, Peng Wang, Rajesh Menon, Rosa M. Trejo, Edgar Lara-Curzio, Scott R. Hunter, John T. Simpson, M. Parans Paranthaman and David K. Christen*

[*] T. Aytug, A. R. Lupini, G. E. Jellison, P. C. Joshi, I. N. Ivanov, T. Liu, R. M. Trejo, E. Lara-Curzio, S. R. Hunter, J. T. Simpson, M. Parans Paranthaman, D. K. Christen

Oak Ridge National Laboratory

Oak Ridge, TN 37831 (USA)

E-mail: aytugt@ornl.gov

R. Menon, P. Weng

Department of Electrical and Computer Engineering

The University of Utah

Salt Lake City, UT 84112

A revolutionary impact on the performance of many optical systems and components can come from the integrative design of multifunctional coatings. Such coatings should be mechanically robust, and combine user-defined optical and wetting functions with scalable fabrication formulations. By taking cues from the properties of some natural biological structures, we report here the formation of low-refractive index antireflective glass films that embody omni-directional optical properties over a wide range of wavelengths, while also possessing specific wetting capabilities. The coatings comprise an interconnected network of nanoscale pores surrounded by a nanostructured silica framework. These structures result from a novel fabrication method that utilizes metastable spinodal phase separation in glass-based materials. The approach not only enables design of surface microstructures with graded-index antireflection characteristics, where the surface reflection is suppressed through optical impedance matching between interfaces, but also facilitates self-cleaning ability through modification of the surface chemistry. Based on near complete elimination of Fresnel reflections (yielding > 95% transmission through a single-side coated glass) and corresponding increase in broadband transmission, the fabricated nanostructured surfaces are found to promote a general and an invaluable ~ 3-7% relative increase in current output of multiple direct/indirect bandgap photovoltaic cells. Moreover, these antireflective surfaces also demonstrate superior resistance against mechanical wear and abrasion. Unlike conventional counterparts, the present antireflective coatings are essentially monolithic, enabling simultaneous realization of graded index anti-reflectivity, self-cleaning capability, and mechanical stability within the same surface. The concept represents a fundamental basis for development of advanced coated optical quality products, especially where environmental exposure is required.

1. Introduction

Suppression of light reflection from glass surfaces is a critical consideration for improved performance in numerous and diverse optical applications. Due to step discontinuity in refractive index, about 4% of light is reflected (essentially lost) from each air/glass interface. To suppress these undesirable, so-called Fresnel-reflections, various designs of antireflective (AR) coatings are implemented extensively in a wide variety of optical systems. As such, AR coatings can: (i) raise the efficiency and power output of the photovoltaic devices[1,2]; (ii) enhance the light extraction from light emitting diodes[3]; (iii) increase transmissivity and eliminate unwanted ghost images in flat panel displays, architectural windows and lenses[4,5,6,7]; (iv) reduce background noise, thereby increasing the sensor performance in imaging systems and detectors[8,9]; and (v) minimize the reflection induced failure of laser components in high-power laser systems[10,11]. To realize the full potential of AR coatings, it is highly desirable that the coated optical element provide spectrally broadband reduction in reflectance over a wide range of incident angles. However, there exists no single inorganic optical material with a low index of refraction (i.e., close to that of air, n=1) that can be applied to any glass platform to enable broadband and omnidirectional AR characteristics. Traditional single or multilayer step-index AR coatings either target only a limited spectral range and have narrow field of vision, or exhibit broadband anti-reflectivity but suffer from high-cost due to low-throughput complex fabrication processes[12,13]. Recently, much of the research on broadband and omnidirectional AR coatings has focused on layered designs or creation of subwavelength structures, often inspired from biological surfaces, where the refractive index varies step-wise or continuously from the ambient medium to the substrate[14,15]. However, commercially such graded-index-coatings presently are very challenging, being mainly based on either expensive, elaborate and limited resolution top-

down lithography techniques (e.g., photolithography, e-beam lithography, nanoimprint lithography, interference lithography) [16,17,18,19,20] or on bottom-up approaches (e.g., colloidal self-assembly, anodic alumina films, carbon nanotubes), [21,22] or a combination of both. [23] While the latter methods can be relatively cost-effective, they are mostly pertinent to laboratory-scale fabrication. Moreover, coatings based on both general approaches have a propensity to exhibit poor mechanical and thermal stability, impeding the integration into large-scale development and production.[21] In addition to AR attributes, coatings also should often possess environmental stability and multifunctional surface characteristics, especially for integration into systems that have extended operational exposures to extreme climates including humid conditions or dust prone environments. In these cases, great benefit will be derived from self-cleaning and/or anti-fogging functionality of the coatings (e.g., for solar cells, lenses, sensors, photodetectors, architectural windows, etc.).[24,25,26,27]

In this study, we demonstrate a novel approach that enables dramatic suppression of light reflection losses at glass-air interface over a broad range of wavelength (λ) and incident angles. The present technique exploits material phase-separation through spinodal decomposition in low-alkali borosilicate glass systems to produce porous, nanostructured graded refractive index AR glass film coatings with self-cleaning and antifogging capabilities.[28,29,30] When simulated as a cover glass on various solar cells having different band gaps, these nanostructured glass surfaces enabled substantial gains in light-to-electricity conversion efficiency, compared to uncoated counterparts. Unlike other step-index AR coatings, the present monolithic coating has a controllable porous submicron structure that offers game-changing advances, such as tunability of the refractive index, ability to optimize the coating for any glass substrate-ambient material

system, tailored wettability, and compatibility with current industrial scale manufacturing practices.

2. Results and discussion

The basic approach to fabrication begins with deposition of a glass coating that will spinodally (i.e., non-nucleation, continuous phase separation) decompose when properly thermally processed. Following film deposition by magnetron sputtering onto transparent substrate platforms, the subsequent heat treatment renders the glass coating phase separated into an interpenetrating pattern consisting of alkali-borate-rich and a silica-rich phases, the former being relatively more soluble by a variety of chemicals. Subsequently, a controlled level of differential etching is employed to selectively dissolve the sodium-borate-rich phase, leaving behind a porous three-dimensional reticulated network of high-silica content glass phase. Figure 1 illustrates the general stages of coating fabrication. Since the spinodal phase separation is a kinetically driven diffusion controlled process, for a given glass composition the structure and dimensions of the resultant phases and matrix microstructure are controlled by the heat treatment temperature and time, combined with the etch conditions (i.e., etchant type, concentration, and etch duration). Interplay among such processing parameters enables ability to tune the microstructural features of the films for tailored performance. In Figures 2a-c are the scanning electron microscopy (SEM) images, illustrating the morphological evolution of the differentially etched spinodal film structure with respect to different heat treatment durations. Clearly, for a given heat treatment temperature (i.e., 700 ^{o}C in this case), prolonged processing time within the metastable immiscibility region of the SiO_2-B_2O_3-Na_2O system results in larger spinodal features (i.e., size of the silica skeleton) and a size distribution of the pore structure that is correlated with the dimensions of the etched out sodium borate phase.

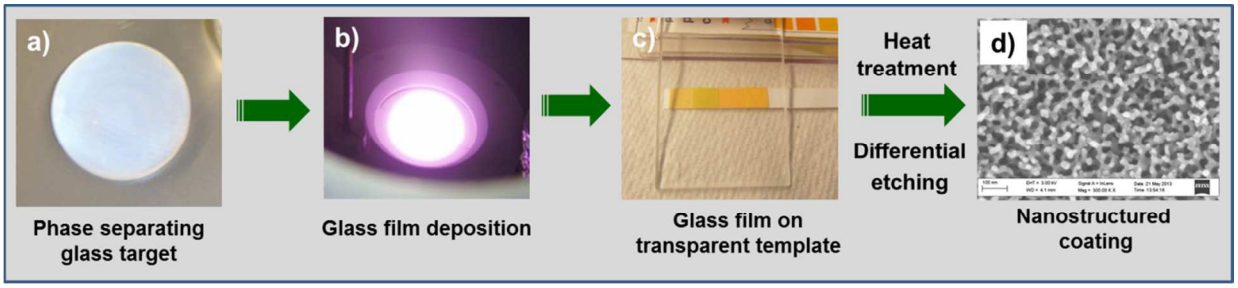

Figure 1 (color online). Preparation of nanostructured silica films. a) specially formulated sputtering target, b) deposition during magnetron sputtering, c) photograph of the sputter-coated glass substrate (coated side is facing up and it is not possible to distinguish it from the uncoated side), d) high resolution scanning electron microscopy image showing the nanostructured surface morphology of the coating after the post-deposition treatments (scale bar in the image represents 100 nm).

Since the two phases are completely intertwined, a prolonged exposure to the etchant solution gradually leads to the expansion of pores deep into the film matrix. In fact, the corresponding 'Z-contrast' cross-sectional scanning transmission electron microscopy (STEM) images (Figures 2d and e, for the same samples as presented in Figures 2a and 2c) reveal the interpenetrating nature of the pores, as well as highlight the very different, heat treatment time dependent, size distribution of SiO_2-skeleton/pore-structure throughout the film thickness. Note that the higher-Z elements (Si with Z = 14) appear brighter than the lower-Z elements in this imaging mode, revealing darker porous areas and brighter regions of mainly SiO_2 phase. Whether the films are partially (Figure 2d) or completely etched (Figure 2e), the notable microstructural differences among the samples underscores the tunability of the present approach for the production of tailored nanostructured optical coatings. In particular, formulations that would enable simultaneous realization of excellent water-repellency and suppression of light scattering losses would convey significant value for a variety of devices. Generally, the requirements of surface roughness for water-repellency, super-hydrophobicity, and optical functionality present competing constraints.

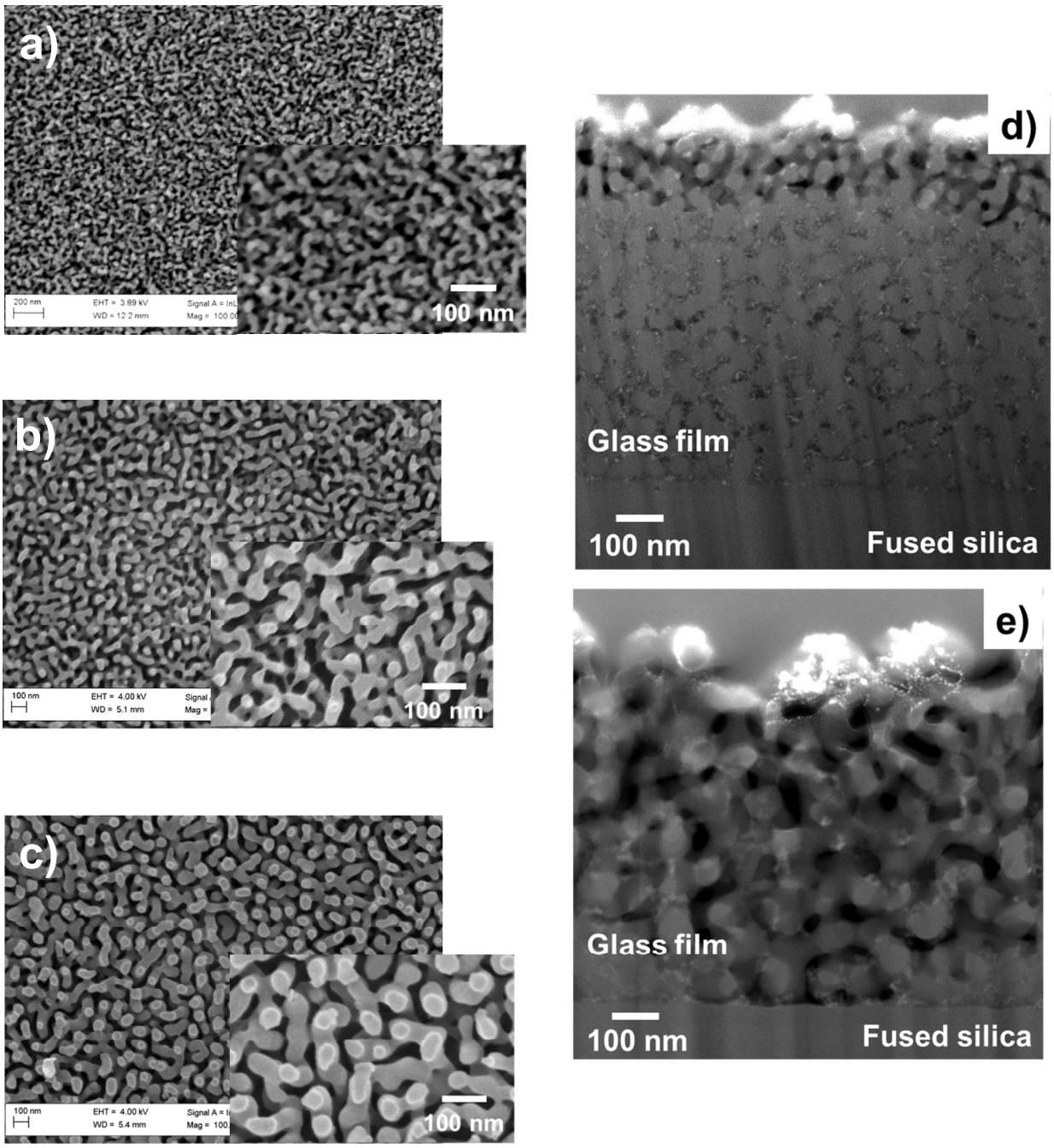

Figure 2. Scanning electron microscopy images of fully processed, phase separating glass films on fused silica substrates at different heat treatment periods. Note that heat treatment temperature (710 ^{o}C) is kept identical for all samples. Heat treatment times are: (a) 5 min, (b) 30 min, and (c) 120 min. Images highlight the reticulated nature of the phase separation. Insets show the higher magnification images. Cross-sectional morphologies (d) and (e) of the same samples in parts (a) and (c), respectively. These Z-contrast images display the three dimensionally interconnected landscape of the pores and the silica-rich film matrix throughout the coating thickness.

However, as shown in Figure 2 and further discussed below, the unique processing methods have led to coatings with phase separated feature sizes that are much smaller than visible wavelengths, for the attainment of superior optical properties, while simultaneously ensuring extreme non-wetting surface characteristics. Considering the former property – optical functionality – the microstructure of the present coatings can be designed (i.e., by modifying the processing protocols as discussed above) such that the pore fraction and its size can be gradually varied (i.e., progressively reduced), from the air-film interface towards the bulk-film medium, in order to achieve a graded refractive index profile for reduced reflection. An example of such gradation can be observed in Figure 3, which shows the Z-contrast STEM images of a controllably etched silica film deposited on a borosilicate glass template. Clearly, the volume fraction of the pores progressively decreases from the top to the so-called etch front (demarcated with dotted line in Figure 3). Below the etch front, the pores are significantly smaller (see right panel inset) and their fill density continuously declines until the film matrix assumes its unetched dense material structure.

Because the scale of features in the film is much smaller than the wavelength of the visible light, from a fundamental viewpoint the effective refractive index at a certain depth can be approximated as a set of multiple layers composed of homogeneous mixtures of air and dense film material, weighted in proportion to the volume of the constituents. [31] In order to determine the refractive index profiles of the nanoporous glass films, spectroscopic ellipsometry measurements have been made on a film that was processed under conditions similar to those of the sample shown in Figure 3. We utilized the Levenberg-Marquardt fitting procedure, determining the χ^2 as a figure of merit where the errors of the data are included as described in

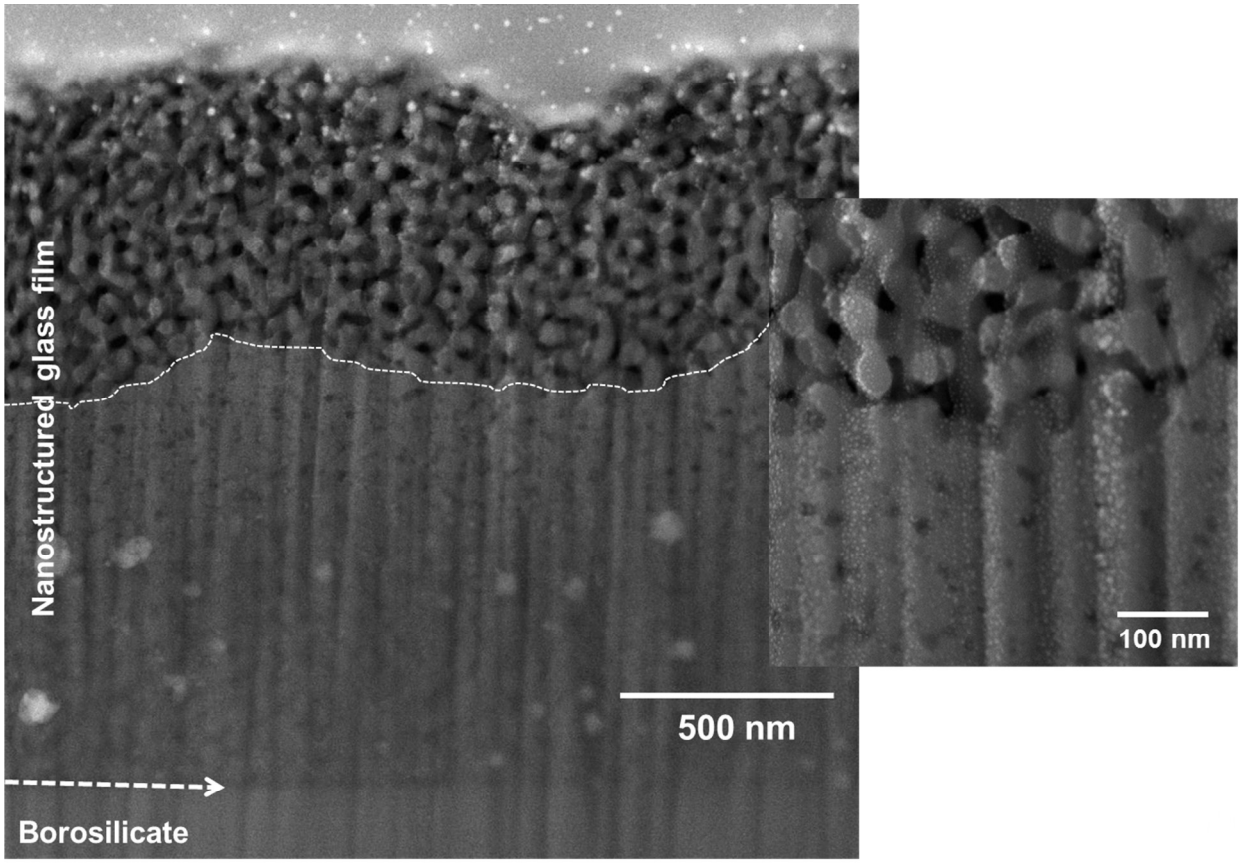

Figure 3. Cross-sectional Z-contrast STEM image of a partially etched glass film (2000 nm thick). The etch-front is marked by the dotted line. The sample is annealed at 625 ^{0}C for 60 min. Dashed arrow denotes the interface between the film and the substrate. Right inset shows a higher magnification view in the vicinity of the etch-front, illustrating the microstructural differences above and below the etch-front.

references [32] and [33]. The model film structure consists of five media: air/interface-1/film/interface-2/glass-substrate. The optical functions of interface-1 and interface-2 were determined using the Bruggeman effective medium approximation [34], consisting of 50% of the medium above and 50% of the medium below. The film and the glass substrate optical functions were modeled using the Sellmeier approximation, where the dielectric functions (or refractive indices) are given by

$$\epsilon = n^2 = 1 + \frac{A\lambda^2}{\lambda^2 - \lambda_o^2} \quad . \qquad (1)$$

In equation (1), n is the refractive index, λ is the wavelength of light, and A and λ_o are fitted parameters. Details of the fitting procedure are given in the supplementary document.

The simplest model consisted only of air, film and the substrate, where the interfacial film layers were not taken into account. For this fit, the resulting $\chi^2 = 23.0$ was excessively high. When the interfacial layers are added to the analysis, then the χ^2 value reduced to 11.8. The best fit to the data was obtained using a seven-parameter fit, where a Gaussian distribution over the parameter A_{film} was included for the film. The distribution is used to simulate the variation in the optical functions that the ellipsometer samples over the spot size (~ 3 mm × 5 mm) with varying refractive indices.

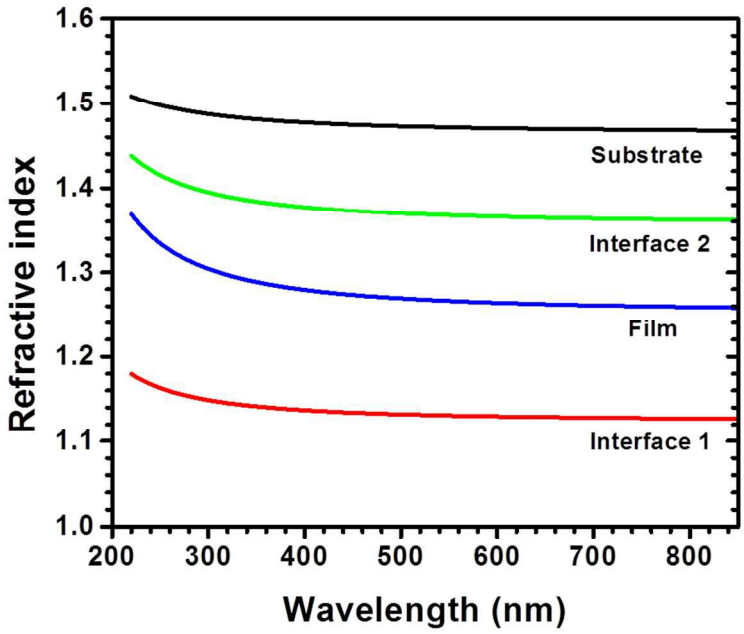

Figure 4 (color online). The spectroscopic refractive index of the various layers for the model described in the text, illustrating the gradual change of the refractive index from substrate to air.

In addition, $A_{substrate}$ was also included into the mix as a fitting parameter, since the ellipsometric measurement is highly sensitive only to the etched porous top-most region of the coating. Any

small microstructural changes to the near-surface region of the substrate (or even the dense film section) will not be well represented by the optical functions of the untreated glass substrate. Taking all these considerations into account, the χ^2 was substantially reduced to 4.5, where the fitted data are displayed in supplementary Figure S1 and the fitted parameters with errors are documented in supplementary Table ST1. Further attempts to improve the fit resulted in very small reductions in χ^2, but with much larger cross correlation coefficients, making these results less reliable. Although the best χ^2 is greater than 1 and a more complicated model is required, it is clear that the general features of the model are reasonable. Figure 4 shows the resulting spectroscopic refractive index profiles for the three modeled layers (interface-1/film/interface-2), as well as the refractive index of the substrate. The results show that the refractive index of the nanostructured glass film is considerably less than that of the bulk glass. Moreover, the refractive index is graded such that the near surface refractive index is very close to that of the air (n = 1.0) and the refractive index of interface-2 is between the film and the substrate, making the AR properties even more effective. In fact, a general variation in the refractive index with depth is established, where the refractive index progressively increases with depth into the film, finally assuming the substrate value. Accordingly, these two combined property enhancers – attainment of a very low index of refraction and tailoring of the refractive index through control of microstructure – make the present platform uniquely suited to produce optical coatings with the highest possible performance characteristics. In fact, next we show a near-complete elimination of Fresnel reflections from the single-side coated glass over a broad wavelength and angle-of-incidence range. Wavelength-dependent near-normal incidence transmittance measurements

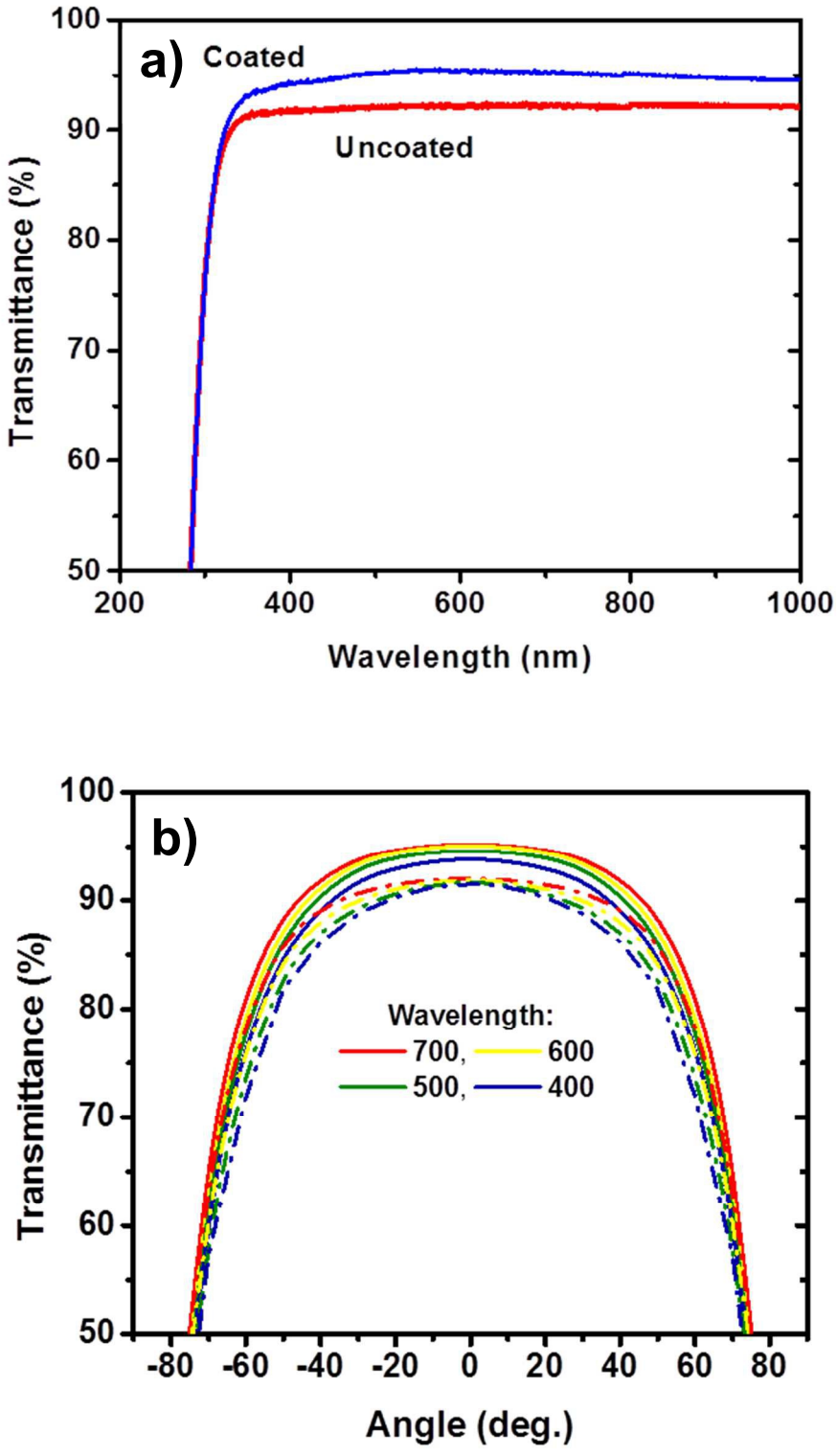

Figure 5 (color online). (a) Wavelength-dependent and (b) angle-dependent optical transmittance spectra of a borosilicate substrate with and without the nanoporous anti-reflective silica film coating. The dashed lines in (b) represent the spectra of the uncoated borosilicate reference.

(obtained on the same sample as presented in Figure 4) revealed significantly enhanced transmittance over a spectral range of 300-1000 nm, compared to that of the underlying reference borosilicate template, remaining on the average above 95.2% (versus ~92%) within the entire visible regime (Figure 5a). Figure 5b illustrates the omnidirectional characteristics of the same sample at specific discrete wavelengths covering the visible spectrum. The measurements were carried out over a range of incidence angles from 0^o to 80^o in 10^o increments, and exhibit increased transmittance through the nanotextured porous surface, compared to that of the unstructured counterpart, for incidence angles up to 70^o. While light transmission through the coated substrate is always greater than the uncoated counterpart, the performance shows sensitivity to the angle of incidence due to the Fresnel reflections from the rear side. For the single-sided nanotextured surfaces, the transmission is limited by reflections arising from the abrupt change in refractive index from the uncoated back surface. In fact, according to theoretical analysis, nearly angle-independent performance could be obtained if the nanostructured coating is applied to both sides of the substrate to eliminate the contribution of the uncoated side.[35] While efforts in this area are currently underway, it is noteworthy that the observed improved light transmittance characteristics of the present coatings are a direct consequence of the reduced surface reflections. To provide further insight into this behavior, as well as to evaluate the effects of light scattering from the nanostructured surface, the specular and diffuse reflectance spectra of the same nanostructured silica film were measured between 200 to 2000 nm, using an integrating sphere. The total reflectance was measured at an incident angle of 3.3^o, where both the specular beam and the scattered light are collected. The diffuse reflectance was collected with the beam normal to the sample surface. The specular reflectance was determined by subtracting the diffuse reflectance from the total reflectance. In accord with

the transmittance results, wavelength-dependent spectra, shown in Figure 6a, reveal that the specular reflectance of the coated glass, relative to the uncoated reference sample, is significantly suppressed over the entire spectrum. Notably, in the visible range of the spectrum, the reflectance is reduced by ~75-85% relative to the underlying flat template. For high performance antireflective characteristics, not only the specular reflectance but also the diffuse reflectance from the coating surface should be minimized, especially for surfaces having a roughness profile.[36] Figure 6b illustrates the diffuse reflectance spectra of the same samples. Except at shorter wavelengths (i.e., ≤ 300 nm), the nanostructured silica coating enables lower reflectance over the entire spectral range, indicating that the observed reduction in specular reflectance (Figure 6a) is not caused by the light scattering associated with the surface roughness of the etched glass film, but arises merely from the optical impedance matching between air and the substrate interfaces. Note that, although the final material character in both the coating and the substrate is similar, the fact that the coating is not dense and has a porous submicron structure, with dimensions gradually changing through the thickness, significantly changes its effective index of refraction (see Figure 4). From a fundamental standpoint, performance can be modeled as a nanostructural-modulated refractive index gradient (i.e., the closer to the substrate, the higher the index), which decreases reflection because there are no abrupt index changes.[37] Hence, the final etched-out film structure functions as a true graded-index anti-reflective coating. The combined results of enhanced transmission and reduced reflection over a broad spectrum, as well as the applicability of these coatings to a wide variety of glass platforms, would significantly benefit just about any application where light travels into or out of a material. In particular, for photovoltaic panels the light energy lost to reflection can be substantially reduced; this directly increases the light coupling into the solar cell, promoting the energy yield of the

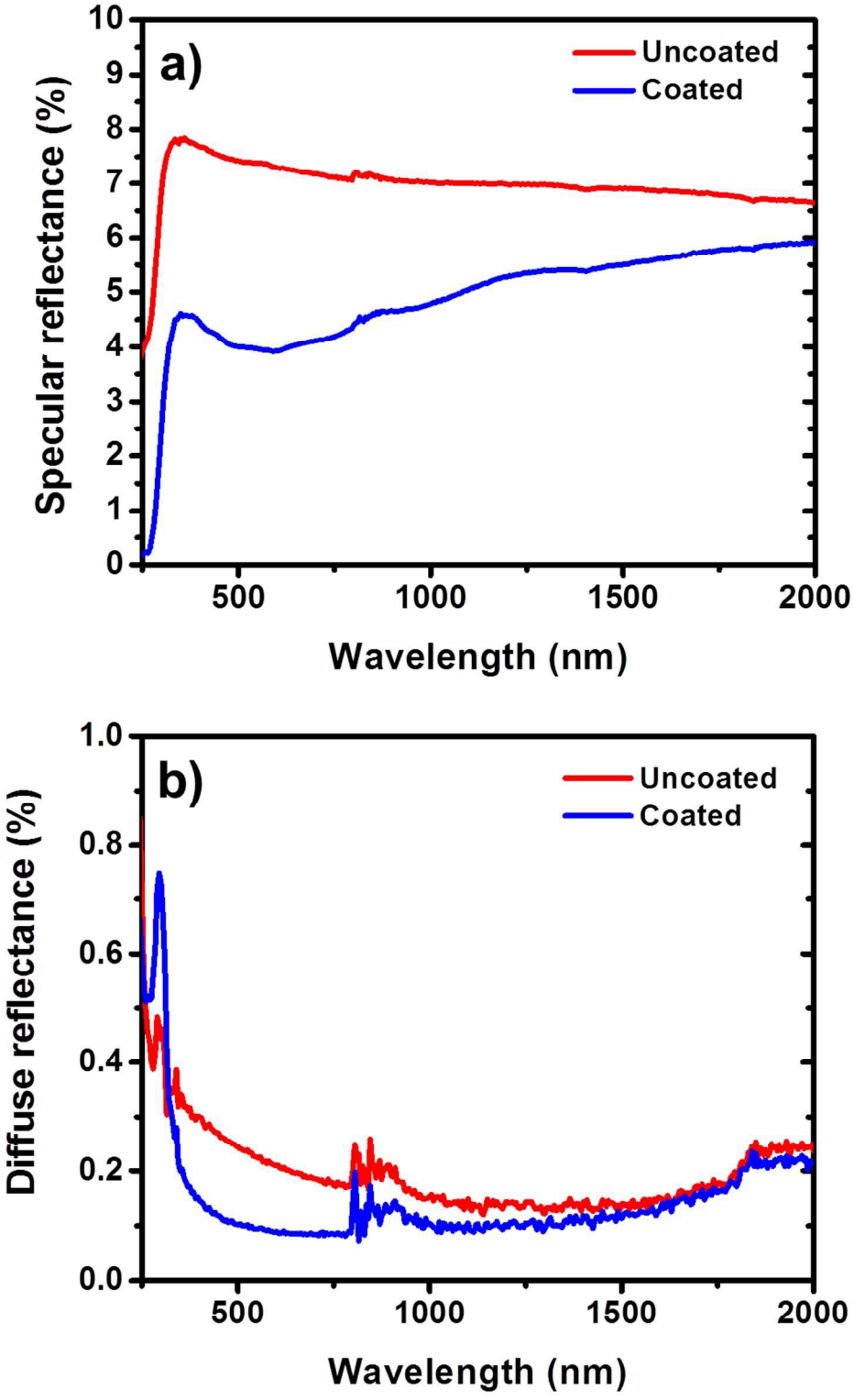

Figure 6 (color online). Comparison of the wavelength-dependent spectra for (a) specular reflectance and (b) diffuse reflectance of the same samples as presented in Figure 5. The spectral features around 800 -900 nm is an instrumental artifact, due to the switching of the detector.

Table 1. Summary of the short-circuit current densities of the GaInP (E_g = 1.84 eV), GaAs (E_g = 1.42 eV), Si (E_g = 1.12 eV), and CuInGaSe (CIGS, E_g = 1.42 eV) solar cells. For the measurements, coated (sample) and uncoated (reference) borosilicate substrates were placed in front of the photovoltaic cells to simulate the outer protective cover glass. The relative gain in short-circuit current densities (labelled as boost) for each cell is also listed.

	J_{sc} [mA/cm^2]	Boost
	GaInP	
Reference	**0.5438**	**6.60%**
Sample	**0.5797**	
	GaAs	
Reference	**0.8157**	**6.20%**
Sample	**0.8663**	
	Si	
Reference	**0.4782**	**3.37%**
Sample	**0.4943**	
	CIGS	
Reference	**0.6329**	**5.37%**
Sample	**0.6669**	

module. In conjunction with this, the effectiveness of the nanostructured glass surfaces in enhancing the performance of photovoltaic devices was demonstrated by simulating the coated samples as a protective cover glass on various solar cells having different optical band-gaps (see figure S2 in the supplementary document). The measurements reported here were made using a broadband super-continuum source with the illumination beam collimated to a power density of 3.42 mW/cm^2 (see experimental section for the details of the measurements). The same coated and uncoated samples, as represented in Figures 4, 5 and 6, are portrayed as the cover glass. In Table 1, the short-circuit current densities (J_{sc}) of the cells, with and without the nanostructured silica coatings, are compared; and the relative improvements in performance, termed as "boost", are summarized. As anticipated, the increased light transmission, resulting from the graded index

antireflective effect, leads to substantial enhancement in J_{sc} (i.e., ~ 3-7% relative increase) for a diverse selection of direct and indirect bandgap solar cell devices. Hence, unlike other antireflective technologies, independent of the device chemistry or microelectronics design, the present technique offers a practical solution to improve the performance of the photovoltaic modules simply by integrating a thin layer of monolithic material onto the protective glass surface.

In order to maintain the light-to-current conversion efficiency of the outdoor photovoltaic panels it is also crucial to prevent soiling of the cover glass surface by the accumulation of sand, dust, and other pollutants.[38] The accumulated buildup of contaminants on the panels can result in energy losses reaching to 15%.[39] One of the approaches to generating a self-cleaning surface is based on the principle of superhydrophobicity, induced by the combination of unique surface nano-/micro-structures and the surface chemical composition [40,41,42]. This physicochemical fine surface construction traps a thin layer of air, which greatly reduces the area of contact between a water droplet and the roughened surface, thus preventing penetration of water into the surface structure. Akin to many non-wetting biological systems (e.g., lotus leaves and water strider legs), on such artificially created superhydrophobic surfaces the water droplets can effectively clean the surface due to the much weaker adhesion between the contaminant particles and the superhydrophobic surface compared to the water droplets and the particle. Prior to modification of the surface chemistry, the fabricated silica films, with approximate pore sizes of 10–20 nm, qualitatively demonstrate structural super-hydrophilicity. This promotes antifogging characteristics by allowing condensation to rapidly spread and wet the surface, in part through capillary action and in part due to the hydrophilic nature of the Si-O-Si network, as has been

elucidated in our previous report.[43] On the other hand, by simply changing the surface chemistry with low surface energy functional groups, these textured AR coatings

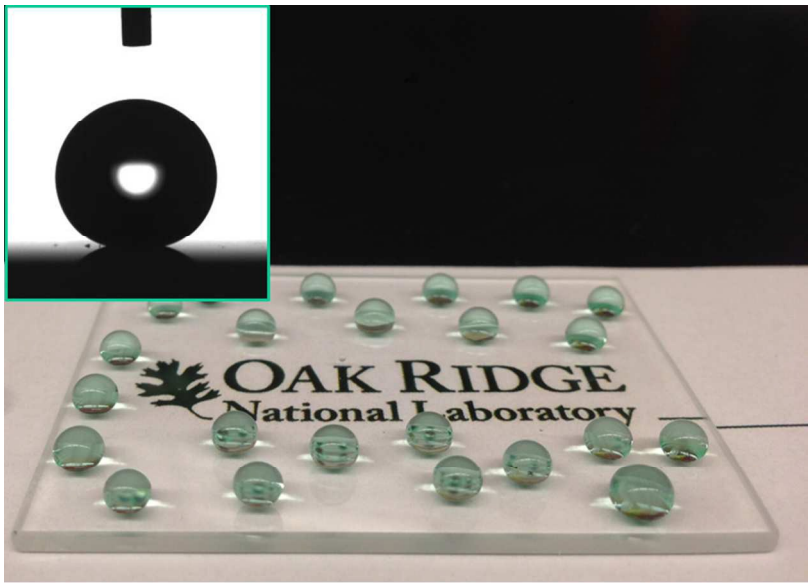

Figure 7 (color online). Photograph of blue dyed water droplets on a borosilicate substrate coated with nanoporous antireflective glass film. The film surface is modified by a covalently bonded organosilane chemistry. Inset shows the profile of a 5 μl water droplet resting on a similarly processed film, displaying a static contact angle of 165°.

support exceptional superhydrophobicity, where the static water droplet contact angle (CA) values extend to as high as 165° (Figure 7). The water droplets on these surfaces assume a nearly spherical shape (see inset of Figure 7) and roll off very easily at a tilt angle < 5°. This implies that the water droplets do not penetrate into the porous silica film matrix, but instead are suspended on the mixed interface composed of the surface asperities, which are 10-100 nm apart, with air pockets trapped between them. Consequently, these surfaces demonstrate an intrinsic water-proof property and self-cleaning ability (discussed below in more detail); which is important not only for solar modules but also for other devices and surfaces that are exposed to typical environmental encumbrances.

Another significant merit of these nanostructured silica coatings is their mechanical and structural robustness. In particular, scratch and abrasion resistance are two important measures by which to assess the adhesion strength of a coating, as well as its resistance to permanent plastic deformation. The structural integrity of the coatings was assessed by conducting two complementary tests. The first test was performed by using a nanoindenter to qualitatively evaluate the relative scratch resistance as well as the adhesive strength of the coatings to the underlying glass platform. Through this procedure, a critical load (if any) can be established at which the material fractures or undergoes permanent plastic deformation. Films approximately 1 μm in thickness were fabricated on borosilicate glass templates and a conical indenter with a tip radius of 1 μm and cone angle of 90^{o} was used for the measurements at ramping loads. Figure 8a shows typical indenter generated scanning probe microscopy images of scratch tracks for a sputter deposited film, a fully processed film (i.e., heat treated and etched), and the underlying borosilicate substrate. The scratches, produced after the application of load ramped up to the equipment peak of 10,000 μN, showed no evidence of cracking, brittle fragmentation or tendency toward delamination. Moreover, for loads at one-half and at full equipment maximum the average penetration depth (calculated from the lateral and vertical displacements) of the indenter is nearly the same for both the reference substrate and the coated sample (Table 2). This result suggests that the scratch resistance behavior of the as-deposited films is similar to that of the underlying substrate material. Accordingly, the coefficient of friction profiles for a representative template revealed similar behavior, as displayed in Figure 8b. It is important to note that no accurate penetration depths could be measured for the etched samples due to a surface roughness (~ 300 nm) that is nearly equivalent to the depth of the scratch grooves. It can also be inferred from Table 2 that the scratch characteristics of the films on fused silica platforms

are very similar to those obtained on borosilicate counterparts. Slightly larger scratch depths for the coated samples indicate a softer nature of the glass films relative to the underlying substrate materials. In fact, hardness measurements performed on the same samples, using a Berkovich

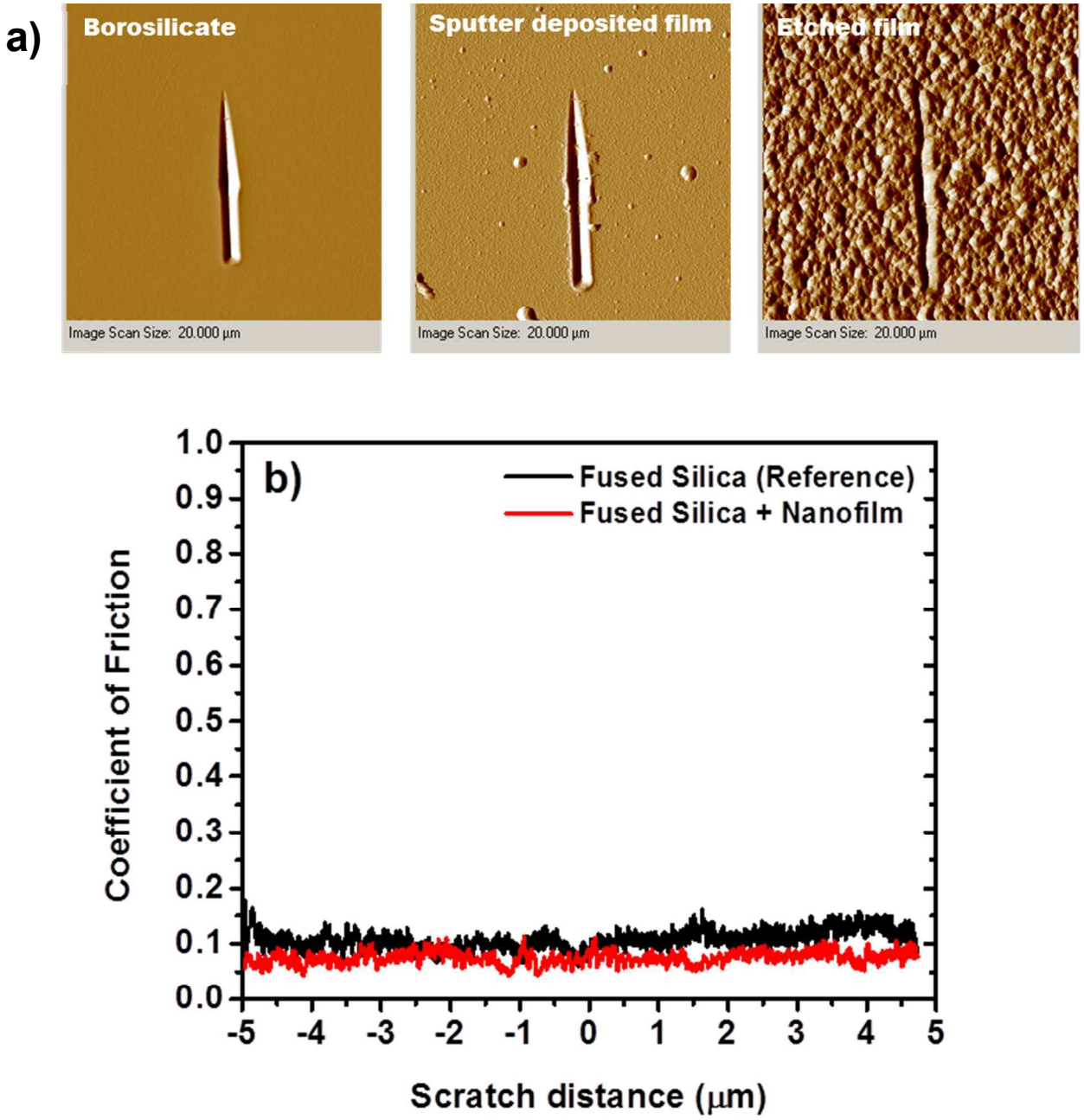

Figure 8 (color online). (a) Topographical images of the scratches made on an as-deposited and a nanotextured glass thin film. Image for the underlying uncoated borosilicate substrate is also included for comparison. No debris is observed on any sample, aside from several small and

large sized surface-bound particles on the sputtered film. Note that the as-sputtered borosilicate films are generally somewhat rougher than the underlying substrates. (b) Comparison of the coefficient of friction profiles as a function of scratch distance for fused silica substrates with and without a dense borosilicate film.

Table 2. Average penetration depths of the conical indenter during the scratch tests for the coated and uncoated glass substrates. Data are listed at half and at the peak load of the equipment maximum.

Sample	Penetration Depth at 5000 µN [nm]	Penetration Depth at 10000 µN [nm]
Fused silica	227.5 ± 1.56	342.53 ± 0.87
Film on fused silica	236.67 ± 3.27	344.4 ± 0.99
Borosilicate	254.18 ± 0.7	384.03 ± 1.96
Film on borosilicate	270.73 ± 4.25	403.1 ± 1.41

indenter, confirmed that the glass films, under a light force of 1.4 mN, are indeed softer than the substrate materials. Nevertheless, it is expected that the fully processed films may be more forgiving to scratch induced damages, because their porous microstructure should provide relatively lower interfacial and residual stresses than the as-deposited dense films.

Following scratch tests, environmental stability as well as the self-cleaning property of the AR films were evaluated by performing Al_2O_3 impact abrasion tests. In this test, real outdoor field conditions (e.g., harsh desert environment with sand storms) are simulated based on a report provided by National Oceanic and Atmospheric Administration (NOAA).[44] Employing the test procedure described in our previous report,[43] a superhydrophobic AR sample on a fused silica platform was blasted with sharp and rugged-edged Al_2O_3 particles at a velocity of 80 km h^{-1} for 15 min. This impact velocity corresponds to an impingement energy of ~ 6 x 10^{-7} J per particle (see videos SV1 and SV2 in the supplementary document), the maximum that was recited in the

NOAA report. After this extremely abrasive test, the nano-silica film retained water repellent (see supplementary video SV3) and self-cleaning properties (Figure 9b), with a slightly reduced CA of 149°, down from 155°. The reason for this slight degradation is attributed to the formation of impact generated defects on the film surface that also led to increase in light scattering and substantial loss of light transmissivity. Figure 9a shows the optical transmittance through the nanostructured film after the abrasion test, including data for uncoated fused silica and borosilicate glass reference materials.

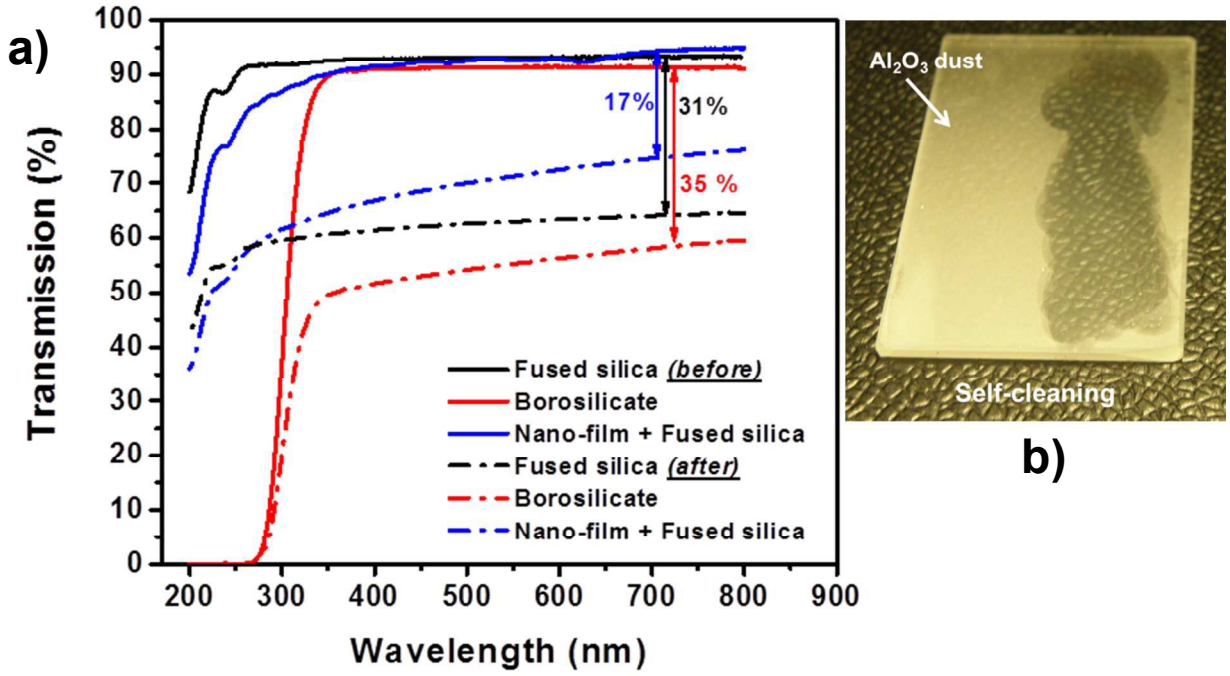

Figure 9 (color online). (a) Specular transmission spectra of a sputter deposited and fully processed nanostructured sodium borosilicate film on a fused silica substrate after sand-storm conditions (see supplementary video SV1), simulated using highly abrasive Al_2O_3 particles at 80 km h^{-1}. For comparison, spectra for the uncoated fused silica and borosilicate substrates taken before and after the test are also included. (b) Appearance of the same sample after the impact abrasion test. While the surface demonstrates self-cleaning ability of the coating (water is applied and repelled only from the narrow section as shown in the photograph), a loss in transmissivity through that cleaned section of the sample can be visually observed.

Clearly, the figure displays significantly better post-abrasion transmittance for the coated sample across the entire measured spectrum, when compared to the underlying reference fused silica template. For the coated sample, the relative decrease in transmittance at $\lambda = 700$ nm was estimated as ~17%, while both the uncoated quartz and borosilicate materials sustained severe degradation (at $\lambda = 700$ nm) by more than 30%, rendering those surfaces nearly translucent. Measurements also revealed that the softer borosilicate glass sustained more wear than the harder quartz material. For the coated sample, the retention of water repellence and transmittance after this very aggressive abrasion test is not surprising, due to the continuous and consistent microstructure throughout the entire silica network thickness. Just below the surface damage, the remaining structured coating ensures preservation of hydrophobic attributes as well as reduced scattering losses. This undamaged film layer also protects, and impedes roughening of, the underlying substrate surface. Consequently, flat (un-textured) surfaces, lacking such protection, are more prone to AR degradation, as clearly evidenced from the observations of Figure 9. Finally, it is noteworthy that since a much more aggressive abrasive, Al_2O_3, is used to simulate the outdoor sand/dust-storm conditions (rather than much softer and more natural SiO_2) these nanostructured AR surfaces are expected to exhibit robust properties in even more aggressive, real outdoor environments.

3. Experimental

Fabrication of nanostructured glass films on glass substrates: The deposition of glass film coatings was performed with a radio-frequency magnetron sputtering system using a two inch diameter target that is made from a glass composition comprising 66 mole % SiO_2, 26 mole % B_2O_3, and 8 mole % Na_2O. Depositions were carried out on one side of the glass substrates in a sputter-gas mixture of Ar and O_2 (oxygen/argon =1/3), at a total pressure ranging from 3-10

mTorr. No substrate heating is employed during the depositions and the resulting film thickness was about 1μm. After the depositions, the coated glass substrates were annealed in air at temperatures ranging from 625 ^{0}C to 710 ^{0}C for a series of hold times between 5 min. to 120 min, in order to produce adequate spinodal phase decomposition as well as to investigate the variations in film microstructures. Following heat treatment, the phase separated coatings were differentially etched, using ultrasonic activation, in a dilute mixture of deionized water and 10:1 buffered oxide etchant (v/v, 1 : 0.075) for a duration of 3 - 4 min. This component of the methodology is vital since it enables post-deposition transformation of the phase separated coating into a three dimensional porous nanoscale silica network. During the process the sodium borate phase is eradicated to the desired depth that will satisfy visible-light antireflectivity with graded index profile. To create the added functionality of water-repellency, the nanostructured samples were then immersed in a 0.5 vol.% 1*H*,1*H*,2*H*,2*H*-perfluorooctyltrichlorosilane (Gelest, Inc.,) hexane solution. After 15-30 min of soaking, the samples were washed with isopropyl alcohol to remove the unreacted silane residues and then oven annealed at 115 ^{o}C for 15 min.

Microstructural and optical characterizations: Plan-view surface morphology of the nanostructured films was analyzed by a Hitachi S-4100 high-resolution field-emission type scanning electron microscope. Cross-sectional examinations of the samples were conducted by Z-contrast scanning transmission electron microscopy (STEM). Specimen preparation was carried out by focused ion beam (FIB) methods, and STEM images were recorded using a Nion UltraSTEM operating at 200 kV. Optical transmission measurements were conducted using a Carry 5000 UV-VIS-NIR spectrophotometer at normal incidence. Angle-dependent transmission measurements, with incidence angle defined relative to the surface normal, were collected by rotating the specimen. Reflection measurements were taken with an integrating sphere

attachment, where the sample normal was mounted at an angle of 3.3° with respect to the incident light beam. Spectroscopic ellipsometry data were obtained using a two-modulator generalized ellipsometer (2-MGE) at an angle of incidence of 65.01°. Details concerning the instrument and its calibrations as well as underlying theory of 2-MGE were described previously [45,46].

Electrical property characterizations of the solar cells: The electrical properties of the solar cells were evaluated using a broadband super-continuum source, which produces a spectral distribution close to global radiation AM1.5. The illumination beam is expanded and collimated to an effective area of 20 cm^2, yielding a power density of 3.42 mW/cm^2. The experiments were conducted in the same setup previously employed for testing a lateral multi-bandgap photovoltaic system using a diffraction-based spectral-splitting scheme (i.e., a diffractive optic laterally splits collimated spectrum), which requires a relatively large beam dimension, thereby limiting the illumination power density.[47,48] The solar cell output current and voltage upon illumination were recorded with Keithley 2602A source meter. For the measurements, coated and uncoated borosilicate substrates were placed 1.5 cm in front of the cells.

Contact angle measurements: The static contact angle measurements were performed using an optical tensiometer (Attension Theta model T301, Biolin Scientific, Finland) equipped with a CCD camera. Deionized water droplets around 5 μl applied to at least ten different positions on the surface and contact angles were determined by taking the average of these points. Roll-off angles were established by using an automated tilting stage.

Scratch, hardness and abrasion resistance tests: Coating scratch resistance was evaluated by nanoindentation measurements using a Hysitron Triboindenter (Minneapolis, MN), on films approximately 1 μm in thickness. A linear ramp-load scratch test was used to conduct five tests

on each sample. Measurements were made on as-deposited films (before the heat treatment and differential etching steps), on the final etched product as well as on an uncoated reference borosilicate substrate at equipment loads of 5,000 μN and 10,000 μN, the latter of which is the load capability of the instrument. The tests used a conical tip with a radius of 1 μm (90^o cone angle) over a 10 μm long track at a constant velocity of 0.33 μm s^{-1}. After scratch testing, topographical images of the surface were obtained using the same tip with a very small contact load (< 70 nN). For the determination of coefficient of friction, three scratches on each sample were made at a constant load of 15 μN and for 10 μm displacements. During measurements, lateral and normal displacements as well as the lateral force were recorded. To correct for sample tilt and to establish the surface profile, a ramp load pre-scratch test was performed at a maximum of 8 μN for a distance of 5 μm prior to actual scan. Hardness measurements were carried out at the loading rate of 7.5 nm s^{-1} up to a peak displacement of 75 nm (in order to avoid the effect of the substrate for the film coated samples), where it was held for 5 s and then unloaded completely with the same rate. Indents were made using a Berkovich indenter with a tip radius of 150 nm.

For the abrasion tests, 50 g of commercial sharp and rugged-edged Al_2O_3 particles (~100 - 300 μm in size) were impacted normal to the sample surface at a velocity of 80 km hr^{-1} for 15 min using an in-house made apparatus, as described in reference [43]. The particle velocity was determined from wind speed measurements using a hot wire anemometer (General Tools model CIH20DL).

4. Conclusions

In summary, by exploiting vapor deposition of and metastable spinodal phase separation in low-alkali borosilicate glass coatings, we have demonstrated formation of nanostructured films on glass platforms that simultaneously provide graded-refractive-index anti-reflectivity and self-cleaning capability. The three-dimensionally interconnected nanoporous glass coatings significantly suppress Fresnel reflections and provide enhanced transmission over a wide range of wavelengths and incident angles. We have shown that the enhanced optical performance is related to the porosity modulated gradation of the refractive index through the film thickness. The technological potential of these glass coatings is demonstrated through improved light coupling into photovoltaic modules, yielding ~ 3-7% increase in the short-circuit current densities of diverse direct and indirect bandgap the solar cells. Super water-repellency and thus self-cleaning ability of the nanostructured AR surfaces is realized through appropriate chemical modification of the silica film surface energy. Additional experiments demonstrated that these nanostructured coatings are mechanically robust and exhibit superior abrasion resistance. With demonstrated scalable and manufacturable formulations, the present approach can provide an all-in-one combination of multiple salient and unique performance enhancers (i.e., antireflectivity, self-cleanability, mechanical durability), which will benefit a variety of optical device applications, especially those exposed to humid conditions or dust prone environments.

Acknowledgements

This work was supported by the Laboratory Directed Tip Innovation Program of Oak Ridge National Laboratory, managed by UT-Battelle, LLC for the U.S. Department of Energy. STEM research was supported by the U.S. Department of Energy (DOE), Office of Science, Basic Energy Sciences (BES), Materials Sciences and Engineering Division. Mechanical Property

research conducted at High Temperature Material Laboratory, which is sponsored at Oak Ridge National Laboratory by the U.S. DOE Office of Energy Efficiency and Renewable Energy. A portion of this research was conducted at the Center for Nanophase Materials Sciences (CNMS) which is a DOE Office of Science User Facility. Other portions of this research were conducted at the Shared Research Equipment (SHaRE) user facility, which is sponsored at Oak Ridge National Laboratory by the Scientific User Facilities Division, Office of BES, U.S. DOE. Photovoltaic device measurements conducted at the University of Utah were supported by a DOE Bridge award no. EE0005959.

Author contributions

The project was originated by TA; planned and co-ordinated by TA, JTS and DKC. ARL conducted electron microscopy analysis. JCP and INI performed optical characterizations. TL and MPP contributed to material synthesis. GEJ performed spectroscopic ellipsometry measurements and simulations to derive optical parameters. PW and RM carried out electrical property measurements of the solar cells. SRH obtained water droplet contact angle values. RMT and ELC performed and analyzed the mechanical property measurements. TA wrote the manuscript with contributions from DKC and all other authors.

[1] Y.-J. Lee, D. S. Ruby, D.W. Peters, B.B. McKenzie and J. W. P. Hsu, *Nano Lett.*, 2008, **8**, 1501.

[2] M. L. Kuo, D. J. Poxson, Y. S. Kim, F. W. Mont, J. K. Kim and S. Lin, *Opt. Lett.*, 2008, **33**, 2527.

[3] S. J. An, J.H. Chae, G. –C. Yi and G. H. Park, *Appl. Phys. Lett.*, 2008, **92**, 121108.

[4] G.Xu, P. Jin, M. Tazawa and K. Yoshimura, *Sol. Energ. Mater. Sol. C*, 2004, **83**, 29.

[5] J. A. Hiller, J. D. Mendelsohn, M. F. Rubner and J. A. Hiller, J. D. Mendelsohn, M. F. Rubner, *Nat. Mater.*, 2002, **1**, 59.

[6] Y. M. Song, E. S. Choi, G. C. Park, C. Y. Park, S. J. Jang and Y. T. Lee, *Appl. Phys. Lett.*, 2010, **97**, 093110.

[7] T. Okuno, *Proc. SPIE*, International Optical Design Conference, Jackson Hole, 2010, **7652**.

[8] C. Lee, S. Y. Bae, S. Mobasser and H. Manohara, *Nano Lett.,* 2005, **5**, 2438.

[9] A. S. Upadhyaya and P. K. Bandyopadhyay, *J. Phys.: Conf. Ser.*, 2012, **390**, 012018.

[10] L.Vaissié, O. V. Smolski, A. Mehta and E. G. Johnson*, IEEE Photonic Tech L.*, 2005, **17**, 732.

[11] W. H. Lowdermilk and D. Milam, *Appl. Phys. Lett.*, 1980, **36**, 891.

[12] S. Chhajed, D. J. Poxson, X. Yan, J. Cho, E. F.Schubert, R. E. Welser, A. K. Sood and J. K. Kim, *Appl. Phys. Express*, 2011, **4**, 052503.

[13] D. Chen, *Sol. Energ. Mater. Sol.C*, 2001, **68**, 313

[14] S. L. Diedenhofen, G. Vecchi, R. E. Algra, A. Hartsuiker, O. L. Muskens, G. Immink, E. P. A. M. Bakkers, W. L. Vos and J. G.Rivas, *Adv. Mater.*, 2009, **21**, 973.

[15] D. J. Poxson, M.-L. Kuo, F. W. Mont, Y.-S. Kim, X. Yan, R. E. Welser, A. K. Sood, J. Cho, S.-Yu Lin and E. F. Schubert, *Mater. Res. Bull.*, 2011, **36**, 434.

[16] P. B. Chapman and M. C. Hutley, *Nature*, 1973, **244**, 281.

[17] Y. Kanamori, M. Sasaki and K. Hane, *Opt. Lett.*, 1999, **24**, 1422.

[18] Z.N. Yu, H. Gao, W. Wu, H.X. Ge and S.Y. Chou, *J. Vac. Sci. Technol. B*, 2003, **21**, 2874.

[19] P.B. Clapman and M.C. Hutley, *Nature*, 1973, **244**, 281.

[20] K. Hadobás, S. Kirch, A. Carl, M. Acet and E.F. Wassermann, *Nanotechnology*, 2000, 11, 161.

[21] K. Askar, B.M. Phillips, Y. Fang, B. Choi, N. Gozubenli, P. Jiang and B. Jiang, *Colloids Surf., A*, 2013, **439**, 84.

[22] A. Yildirim,T. Khudiyev, B. Daglar, H. Budunoglu, A. K. Okyay and M. Bayindir, *ACSAppl. Mater. Inter.* 2013, **5**, 853.

[23] Z. Huang, M.M. Hawkeye, and M.J. Brett, *Nanotechnology* 2012, **23**, 275703.

[24] H.J. Lee and C. Willis, *Chem. Ind.*, 2009, **21**.

[25] X. Yao, Y. Song and L. Jiang, *Adv. Matter.*, 2011, **23**, 719.

[26] Y. Li, J. Zhang, S. Zhu, H. Dong, F. Jia, Z. Wang, Z. Sun, L. Zhang, Y. Li, H. Li, W. Xu and B. Yang, *Adv. Matter.*, 2009, **21**, 473.

[27] B. G. Prevo, E. W. Hon and O. D. Velev, *J. Mater. Chem.*, 2007, **17**, 791.

[28] W. Vogel, Structure and Crystallization of Glasses, Pergamon, New York, 1971, pp. 60.

[29] M. J. Minot, *J. Opt. Soc. Am.*, 1976, **66**, 515.

[30] D. Enke, F. Janowski and W. Schwieger, *Microporous Mesoporous Mater.*, 2003, **60**, 19.

[31] S. Chattopadhyay, Y. F. Huang, Y. J. Jen, A. anguly, K. H. Chen and L. C. Chen, *Mater. Sci. Eng. R*, 2010, **69**, 1.

[32] G. E. Jellison, Jr., *Thin Solid Films*, 1993, **234**, 416.

[33] G. E. Jellison, Jr., *Thin Solid Films*, 1998, **313**, 33.

[34] D. A. G. Bruggeman, *Ann. Phys., (Leipzig)*, 1935, **416**, 636.

[35] J.A. Dobrowolski, D. Poitras, P.H. Ma, H. Vakil and M. Acree, *Appl. Opt.*, 2002, **41**, 3075.

[36] Y.A Dai, H.C. Chang, K.Y. Lai, C.A. Lin, R.J. Chung, G.R. Lin and J.H. He, *J. Matter. Chem.*, 2010, **20**, 10924.

[37] S. L. Diedenhofen, G. Vecchi, R. E. Algra, A. Hartsuiker, O. L. Muskens, G. Immink, E. P. A. M. Bakkers, W. L. Vos and J. G. Rivas, *Adv. Mater.*, 2009, **21**, 973.

[38] M. Mani, R. Pillai, *Renew. Sust. Energ. Rev.*, 2010, **14**, 3124.

[39] M. Piliougine, J. Carretero, M. Sidrach-de-Cardona, D. Montiel and P. S. Friera, *Proceedings of 23rd EuropeanPhotovoltaic Solar Energy Conference*, Valencia, 2008, 2698.

[40] X.J. Feng and L. Jiang, *Adv. Mater.*, 2006, **18**, 3063.

[41] P. Roach, N. J. Shirtcliffe and M. I. Newton, *Soft Matter.*, 2008, **4**, 224.

[42] B. Bhushan, Y. C. Jung and K. Koch, *Phil. Trans. R. Soc. A*, 2009, **367**, 1631.

[43] T. Aytug, J.T. Simpson, A.R. Lupini, R.M. Trejo, G.E. Jellison, I.N. Ivanov, S.J. Pennycook, D.A. Hillesheim, K.O. Winter, D.K. Christen, S.R. Hunter and J.A. Haynes, *Nanotechnology*, 2013, **24**, 315602.

[44] National Oceanic and Atmospheric Administration, "Dust storms, sand storms, and related activities in the Middle East" April 7, 2003, retrieved from www.magazine.noaa.gov/stories/mag86.htm

[45] G. E. Jellison and Jr., F. A. Modine, *Appl. Opt*., 1997, **36**, 8184.

[46] G. E. Jellison and Jr., F. A. Modine, *Appl. Opt*., 1997, **36**, 8190.

[47] P. Wang, J. A. Dominguez-Caballero, D. J. Friedman and R. Menon, *Prog. Photovolt: Res. Appl*., 2014, DOI: 10.1002/pip 2516.

[48] N. Mohammad, P. Wang, D. J. Friedman and R. Menon, *Opt. Exp.*, 2014, **22**, A1519.

The table of contents entry

A monolithic, graded low-refractive-index antireflective nanostructured glass coating that embodies omnidirectional optical properties over a wide range of wavelengths and possessing specific wetting capabilities is established on glass platforms.

Tolga Aytug, Andrew R. Lupini, Gerald E. Jellison, Pooran C. Joshi, Ilia N. Ivanov, Tao Liu, Peng Wang, Rajesh Menon, Edgar Lara-Curzio, Rosa M. Trejo, Scott R. Hunter, John T. Simpson, M. Parans Paranthaman and David K. Christen*

Monolithic Graded-Refractive-Index Glass-based Antireflective Coatings: Broadband/Omnidirectional Light Harvesting and Self-Cleaning Characteristics